Large variations in volcanic aerosol forcing efficiency due to eruption source parameters and rapid adjustments

Lauren R. Marshall[1], Christopher J. Smith[2,3], Piers M. Forster[2], Thomas J. Aubry[4], Timothy Andrews[5] and Anja Schmidt[1,4]

[1]Department of Chemistry, University of Cambridge, Cambridge, UK

[2]Priestley International Centre for Climate, University of Leeds, Leeds, UK

[3]International Institute for Applied Systems Analysis (IIASA), Laxenburg, Austria

[4]Department of Geography, University of Cambridge, Cambridge, UK

[5]Met Office Hadley Centre, Exeter, UK

Corresponding authors:
Lauren Marshall (lrm49@cam.ac.uk),
Anja Schmidt (anja.schmidt@ch.cam.ac.uk)

Key Points:

- The relationship between volcanic SAOD and ERF depends on the time after an eruption, the eruption latitude and eruption season.

- Rapid adjustments reduce the volcanic forcing by an average of 20% predominantly due to a positive shortwave cloud adjustment.

- We provide a range of global mean volcanic SAOD to global mean ERF conversions dependent on eruption source parameters.

28 **Abstract**

29 The relationship between volcanic stratospheric aerosol optical depth (SAOD) and volcanic
30 radiative forcing is key to quantify volcanic climate impacts. In their fifth assessment report,
31 the Intergovernmental Panel on Climate Change used one scaling factor between volcanic
32 SAOD and volcanic forcing based on climate model simulations of the 1991 Mt. Pinatubo
33 eruption, which may not be appropriate for all eruptions. Using a large-ensemble of aerosol-
34 chemistry-climate simulations of eruptions with different sulfur dioxide emissions, latitudes,
35 emission altitudes and seasons, we find that the effective radiative forcing (ERF) is on
36 average 20% less than the instantaneous radiative forcing, predominantly due to a positive
37 shortwave cloud adjustment. In our model, the volcanic SAOD-ERF relationship is non-
38 unique and varies widely depending on time since an eruption, eruption latitude and season
39 due to differences in aerosol dispersion and incoming solar radiation. Our revised SAOD-
40 ERF relationships suggest that volcanic forcing has been previously overestimated.

41 **Plain Language Summary**

42 Powerful explosive volcanic eruptions inject sulfur gases high into the atmosphere where
43 they form a layer of sulfate aerosol particles that scatter sunlight back into space, decrease the
44 transparency of the atmosphere and cause surface cooling. The amount of sunlight that is
45 scattered depends on the location of the layer of particles and particle size. We have used a
46 complex climate model to quantify how eruptions of different magnitudes and occurring in
47 different seasons and locations, may affect the climate. We find that the relationship between
48 the transparency of the atmosphere and the resulting climatic impact caused by volcanic
49 sulfate aerosol particles depends on the spread of the aerosol and therefore the time since the
50 eruption, the eruption location and the season. Our simulations also show that the eruptions
51 reduce the cooling effect of clouds, which reduces the overall effectiveness of volcanoes at
52 cooling the Earth's surface.

53 **1 Introduction**

54   Volcanic sulfate aerosol, formed in the stratosphere following the release of sulfur
55 dioxide (SO_2) during explosive volcanic eruptions, scatters incoming shortwave radiation and
56 absorbs longwave radiation, which leads to surface cooling that has defined the natural
57 variability in climate over the last millennium (Myhre et al., 2013; Schurer et al., 2013; Sigl
58 et al., 2015).

59   Stratospheric aerosol optical depth (SAOD), which is a measure of the opacity of the
60 stratosphere, is a key property used to estimate the radiative forcing of an eruption. The
61 relationship between the two is a measure of how effective the volcanic aerosol is at forcing
62 climate change and can be used to compare volcanic forcing to other climate forcing agents
63 (Hansen et al., 2005). Traditionally, a constant relationship between SAOD and volcanic
64 forcing is assumed; in the Fifth Assessment Report from the Intergovernmental Panel on
65 Climate Change (IPCC AR5, Myhre et al., 2013), a forcing scaling factor of -25 W m^{-2} per
66 unit change of volcanic SAOD is used. This factor was based on simulations of the 1991
67 eruption of Mt. Pinatubo in the Goddard Institute for Space Studies (GISS) model E (Hansen
68 et al., 2005). Energy balance models and simple climate models (e.g., Haustein et al., 2019;
69 Smith et al., 2018a), which continue to underpin IPCC calculations of radiative forcing and
70 are used in studies that assess the 1.5°C target of the Paris Agreement (e.g., Smith et al.,
71 2019) remain dependent on such conversions. Furthermore, studies that estimate forcing from
72 volcanism on geological timescales (e.g., Landwehrs et al., 2020) rely on using scaling
73 factors to convert SAOD to volcanic forcing.

74   The use of a single scaling factor is problematic for two main reasons. Firstly, the
75 relationship between SAOD and radiative forcing is dependent on several factors such as the
76 cloud cover, surface albedo and insolation (e.g., Andersson et al., 2015). Consequently, the
77 relationship may be dependent on the eruption latitude, the magnitude of the SO_2 emission,
78 emission altitude, and the eruption season as these parameters dictate the location and amount
79 of aerosol that forms (Marshall et al., 2019; Toohey et al., 2011; Toohey et al., 2013), and
80 may differ from that after 1991 Mt. Pinatubo. Secondly, the relationship between SAOD and
81 volcanic forcing depends on how the radiative forcing is calculated; whether this is the
82 instantaneous radiative forcing (IRF) at the tropopause or top of atmosphere (TOA), a
83 stratospherically-adjusted radiative forcing that accounts for changes in stratospheric
84 temperature (e.g., the IPCC AR5 -25 W m^{-2} per unit SAOD value), or the effective radiative
85 forcing (ERF), which accounts for additional radiative effects (termed rapid adjustments) due
86 to changes in the surface land temperature, surface albedo, the tropospheric temperature,
87 water vapor and clouds (Forster et al., 2013; Smith et al., 2018b). Studies have found that
88 when rapid adjustments are included, the total volcanic radiative forcing for large-magnitude
89 eruptions (i.e., 1991 Mt. Pinatubo magnitude) is around 20% weaker than that used in the
90 IPCC AR5, due to positive aerosol-cloud interactions that reduce the magnitude of the
91 negative radiative forcing (Gregory et al., 2016; Larson & Portmann, 2016; Schmidt et al.,
92 2018). However, these studies are based on relatively few historical eruptions, and a
93 systematic investigation into the effectiveness of volcanic forcing across eruptions of
94 different magnitude and with different source parameters has not been conducted.

95 **2 Methods**

96 **2.1 Aerosol-chemistry-climate model simulations**

97   We have used aerosol-chemistry-climate model simulations of a wide range of
98 eruptions that inject SO_2 into the stratosphere to investigate the relationship between SAOD
99 and the ERF. The ERF is the best indication of the resulting temperature response of a
100 particular forcing agent (Forster et al., 2016; Myhre et al., 2013; Sherwood et al., 2015).
101 Simulations were run using the UM-UKCA interactive stratospheric aerosol model, which
102 includes the HadGEM3-GA4 climate model (Walters et al., 2014), the GLOMAP-mode
103 prognostic aerosol scheme (Mann et al., 2010) and interactive whole-atmosphere chemistry
104 as described in Marshall et al. (2019). Volcanic eruptions are simulated by adding an
105 emission of SO_2 so that changes in aerosol number, mass and size are accounted for when
106 calculating SAOD. Prescribed SAOD datasets derived from ice-core-records of sulfate
107 deposition (Crowley & Unterman, 2013; Gao et al., 2008; Toohey & Sigl, 2017) used in
108 previous modelling studies are uncertain and do not include many microphysical and
109 dynamical effects of the aerosol on the resulting optical properties (Toohey et al., 2016). Our
110 simulations were free-running so that aerosol perturbations can feed back onto the model's
111 dynamics, and atmosphere-only with prescribed climatological sea surface temperatures
112 (SSTs) that allow the ERF to be diagnosed (Forster et al., 2016; Smith et al., 2018b). ERF is
113 calculated as the difference in the net (shortwave + longwave) all-sky top-of-atmosphere
114 energy imbalance between the simulation with the volcanic SO_2 emission and a control
115 simulation with no eruption (all other aspects of the two model simulations remain the same).
116 Similarly, we examine the change in SAOD at 550 nm between the two simulations (the
117 volcanic SAOD). The calculation of IRF is outlined in section 2.2.

118   We simulated 82 explosive eruptions with different values of the SO_2 emission,
119 eruption latitude and the emission height, termed 'eruption source parameters', and with half
120 of the eruptions occurring on the 1st of January, and half with the eruption occurring on the 1st
121 of July (with the same combinations of the eruption source parameters). The July simulations

122 are presented in Marshall et al. (2019) and were repeated for this study for the 1st January
123 eruption start date. The value of each eruption source parameter in each simulation was
124 determined using a Latin Hypercube design as described in Marshall et al. (2019) (see their
125 Figure 1), with SO_2 emissions ranging between 10 and 100 Tg of SO_2, eruption latitude
126 between 80°S and 80°N, and a 3-km-deep emission column ranging between 15-18 km and
127 25-28 km leading to very good coverage of the three-dimensional parameter space. The SO_2
128 emissions range from that of 1991 Mt. Pinatubo, estimated to be between 10 and 20 Tg (Guo
129 et al., 2004; Timmreck et al., 2018), to 1815 Mt Tambora (~60 Tg; Zanchettin et al., 2016)
130 and approaching that of 1257 Samalas (~119 Tg; Toohey & Sigl, 2017). Each simulation was
131 run for 38 months following the eruption and was initialized during the easterly phase of the
132 Quasi Biennial Oscillation. We do not run additional ensemble members for each eruption
133 but group the eruptions into subsets in which we analyze average responses focusing on
134 annual and global means that have a low sensitivity to meteorological variability. This is
135 supported by previous UM-UKCA ensemble members of the large-magnitude (~60 Tg SO_2)
136 Mt. Tambora eruption (Zanchettin et al., 2016, Marshall et al., 2018) in which global mean
137 SAOD was very similar.

2.2 Diagnosing instantaneous radiative forcing and rapid adjustments

139 For each of the 82 eruptions we calculate rapid adjustments using the radiative kernel
140 method (Shell et al., 2008; Soden et al., 2008). Differences between simulated responses of
141 surface temperature, atmospheric temperature, specific humidity and surface albedo are taken
142 from each eruption and its corresponding control (January or July) and multiplied by the
143 radiative kernel based on the HadGEM3-GA7.1 climate model (Smith et al., 2020). The
144 kernel converts a perturbation in atmospheric state to a top-of-atmosphere radiative flux
145 based on the latitude, longitude, height and month of the perturbation.

146 For shortwave (SW) cloud rapid adjustments we use the Approximate Partial
147 Radiative Perturbation (APRP) technique (Taylor et al., 2007), which approximates the
148 scattering and absorption of SW radiation through the atmosphere by clouds without
149 specialized model diagnostics. Longwave (LW) cloud rapid adjustments are estimated by
150 substituting cloud fields from each experiment into the base climatology, and vice versa,
151 running both configurations through the SOCRATES offline radiative transfer code (Edwards
152 & Slingo, 1996; Manners et al., 2015), which is the radiation module used in UM-UKCA,
153 and taking the average of the "forward" and "reverse" substitutions. This offline substitution
154 method is akin to a partial radiative perturbation (Wetherald & Manabe, 1988). The IRF is
155 then estimated as the difference between the ERF and the sum of all rapid adjustments (Smith
156 et al., 2018b).
157

3 Results and Discussion

3.1 The relationship between global annual-mean volcanic SAOD and radiative forcing
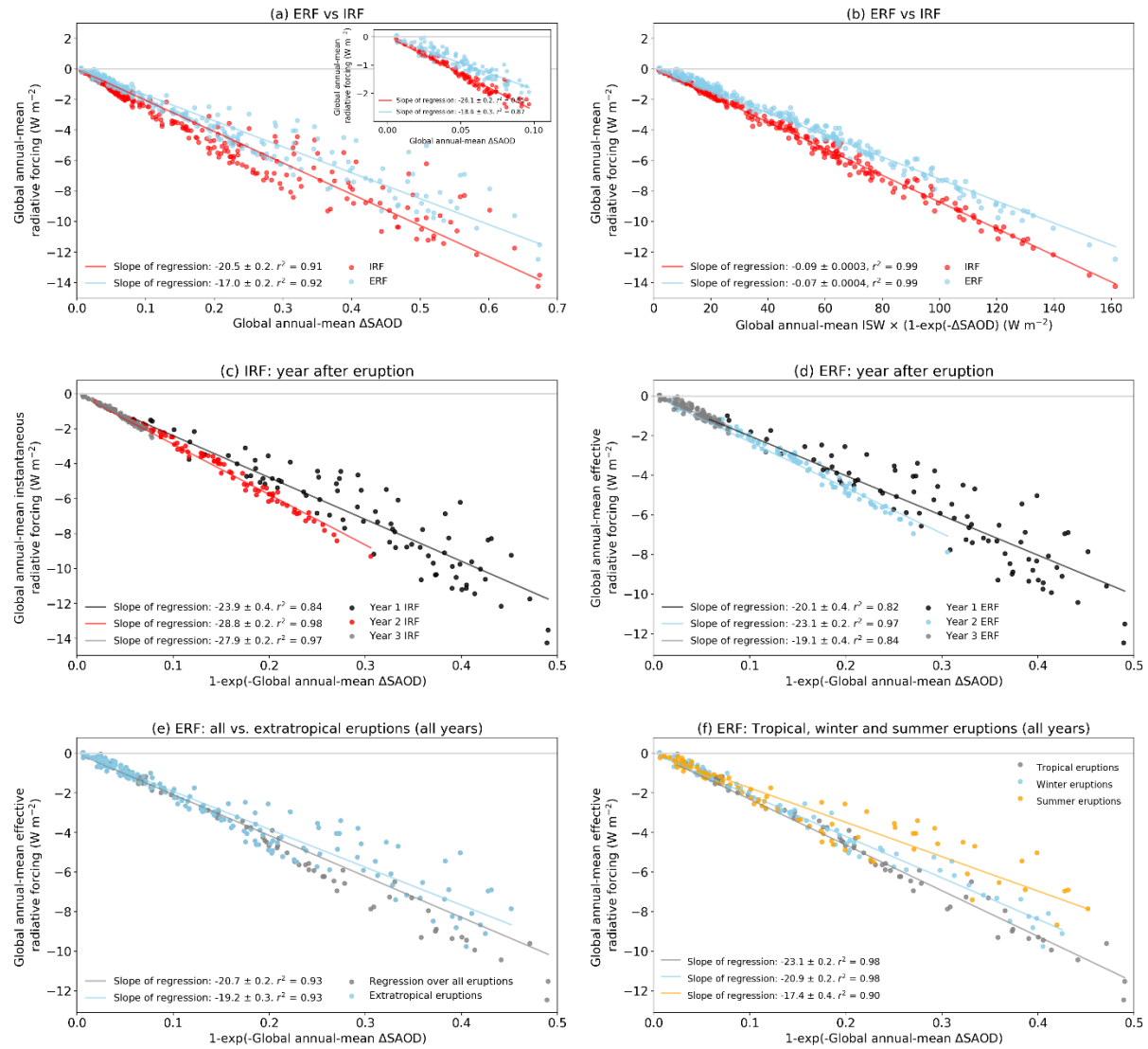

Figure 1. (a) Regression of global annual-mean volcanic SAOD (at 550 nm) against the IRF (red) and ERF (blue) for all 82 simulations. The scatter points show the two quantities in each of the three years after each eruption (82 simulations x 3 years giving 246 data points). The inset shows the regression for SAOD values less than 0.1, upon which the IPCC AR5 scaling factor is based. (b) Global annual mean of 1-exp(-SAOD) multiplied by the incoming shortwave radiation (ISW), against IRF and ERF. (c) 1-exp(-SAOD) against IRF for each year after the eruption. (d) As c, but for ERF. (e) As d, but for all and extratropical eruptions for all years. (f) As d, but for tropical, winter and summer eruptions for all years. The IRF is shown in Figure S1.

Figure 1 shows a series of different regressions to explore the relationship between volcanic SAOD and volcanic radiative forcing. To compare directly with previous conversions, we show first in Figure 1a the global annual-mean volcanic SAOD regressed against both the IRF and ERF for the three years following each eruption across all 82

177   simulations. The slope of each regression line gives the scaling factor in terms of radiative
178   forcing (IRF or ERF) per unit of SAOD. Across all eruptions the IRF is stronger than the
179   ERF, demonstrating that total rapid adjustments are positive, acting to reduce the magnitude
180   of the forcing, in agreement with previous studies (Gregory et al., 2019; Gregory et al., 2016;
181   Hansen et al., 2005; Larson & Portmann, 2016; Schmidt et al., 2018). We explore the rapid
182   adjustments further in section 3.2. Consequently, the IRF scaling factor is larger than the ERF
183   scaling factor, estimated from the regression slopes as -20.5 ± 0.2 W m^{-2} and -17.0 ± 0.2 W
184   m^{-2}, respectively.

185   The linear regression fit for IRF over small SAOD values (<0.1, Figure 1a inset: -26.1
186   ± 0.2 W m^{-2} per unit SAOD) can be directly compared to the IPCC AR5 scaling factor, which
187   is derived from SAOD values also less than ~0.1. Although IPCC AR5 uses the -25 W m^{-2}
188   per unit SAOD factor, additional simulations run with the GISS model E for 1991 Pinatubo
189   using fixed SSTs, produce a scaling factor of -26 W m^{-2} per unit SAOD
190   (https://data.giss.nasa.gov/modelforce/strataer/). Because we also use fixed SSTs in our
191   model simulations, we subsequently use the -26 W m^{-2} factor to compare our results to IPCC
192   AR5 (following Schmidt et al., 2018). Our scaling for IRF over small SAOD values is
193   consequently identical to that of IPCC AR5. Our scaling for the ERF and small SAOD values
194   (-18.6 ± 0.3 W m^{-2} per unit SAOD) is smaller than that calculated by Schmidt et al. (2018)
195   using CESM1-WACCM simulations when regressing for the years 1982-1985 and 1991-1994
196   characterized by the eruptions of El Chichón and Mt. Pinatubo and SAOD also less than ~0.1
197   (-21.5 ± 1.1 Wm^{-2} per unit SAOD; blue line in their Figure 6). This is because we do not
198   include an intercept in our fits so that a zero change in SAOD does not result in a radiative
199   forcing. If we do include an intercept our scaling factor is -20.9 ± 0.7 Wm^{-2} per unit SAOD,
200   which compares very well to Schmidt et al. (2018).

201   The spread around the regression line in Figure 1a collapses if we account for the
202   spatial distribution of the sulfate aerosol and the incoming shortwave radiation (ISW). We
203   first transform the globally and temporally-resolved SAOD to $1-e^{-SAOD}$ (based on a simple
204   application of the Beer-Lambert law) and multiply by the ISW before taking the global
205   annual-mean (Figure 1b). To explore the driving factors of the reduction in this spread,
206   Figures 1c-f show the eruptions categorized according to the year after eruption, eruption
207   latitude and eruption season.

208   We find that the conversion between SAOD and ERF depends on the time after an
209   eruption, eruption latitude and eruption season because of differences in the aerosol
210   distribution and the magnitude of the incoming solar radiation that result in differences in the
211   magnitude of the IRF. Forcing per unit of SAOD is weaker in year 1 than in years 2 and 3
212   with most of the spread in the datapoints arising from year 1 (Figures 1c-d). Forcing per unit
213   of SAOD is stronger for tropical eruptions (between 20°S and 20°N) than extratropical
214   eruptions and stronger for winter eruptions than summer eruptions (Figures 1e-f).

215   In the first year following extratropical eruptions, the aerosol is spatially concentrated
216   in the hemisphere in which it was injected and the IRF depends on the strength of the
217   insolation. This results in a dependency on the eruption season as there is more insolation in
218   the summer hemisphere than the winter hemisphere. Because it takes around 6 months for the
219   aerosol to reach peak burden in our simulations, it is the winter eruptions where more aerosol
220   coincides with high summer insolation resulting in a higher forcing. Zonal mean SAOD and
221   ERF alongside the ISW are shown for each eruption category in Figures S2-4. In the second
222   year after the eruption the aerosol has dispersed more widely, driven by large-scale
223   circulation timescales, which results in a higher global mean albedo for the same global mean
224   SAOD, resulting in a larger global mean forcing per unit of SAOD (but both the SAOD and

225   forcing has reduced by year 2). In addition, depending on the eruption season and latitude, the
226   aerosol may spread to areas with higher ISW, which further enhances the global mean forcing
227   per unit of SAOD. By the third year the aerosol has been largely removed. For tropical
228   eruptions, the aerosol spreads to both hemispheres and is longer-lived as well as coinciding
229   with high tropical insolation resulting in higher SAOD and higher forcing. The dependency
230   on latitude and season is therefore mainly present in the first year after the eruption.

231   The slope of the regressions in Figures 1c-f can be used to convert global annual-
232   mean SAOD (in the form of $1-e^{-SAOD}$) to ERF depending on eruption source parameters.
233   Transforming SAOD to $1-e^{-SAOD}$ removes some of the non-linearity in the data and is chosen
234   here since it is a physically-based quantity that relates to forcing. These conversions are listed
235   in Table S1. Although the global mean conversions cannot explain all the variability
236   discussed above, global annual-mean SAOD remains the most used metric in simple climate
237   models. Importantly, the large range in conversions across the different categories of
238   eruptions illustrates that the SAOD to ERF relationship is non-unique and that the current
239   practice of using a single scaling factor to convert between SAOD and forcing is not
240   appropriate for every eruption.

241   Using the latest reconstruction of global annual-mean volcanic SAOD for the period
242   500 BCE to 1900 CE (EVA(2k): Toohey & Sigl 2017, Figure 2a), we have calculated three
243   different volcanic radiative forcing time-series: 1) By multiplying the global annual-mean
244   SAOD timeseries by the IPCC AR5 factor (-26 W m^{-2}). 2) Converting the global annual-
245   mean SAOD using the all-eruption average relationship we derived here (Figure 1e),
246    $\text{ERF} = -20.7 \times (1 - e^{-SAOD})$. 3) Converting the global annual-mean SAOD using our
247   eruption source parameter (ESP) dependent relationships (Table S1, Figure 1e-f) for tropical,
248   extratropical (if season is unknown), winter and summer eruptions depending on the latitude
249   and season of each eruption from the reconstruction. In this example, annual SAOD values
250   are calendar years. We do not convert EVA SAOD depending on the year after the eruption
251   as the ESP dependent relationships account for a large amount of the variability in the SAOD
252   to ERF conversion (Figure 1f) and the temporal evolution in the EVA reconstruction is based
253   on a simple box model with decay timescales that are different to aerosol-climate models that
254   explicitly account for volcanic SO_2 emissions (Aubry et al., 2020; Zanchettin et al. 2016).

255   The total time-integrated forcing between 500 BCE and 1900 CE using our ESP-
256   dependent conversions is 79% of the total time-integrated forcing when using the IPCC AR5
257   factor (-15977 MJ m^{-2} vs. -20191 MJ m^{-2}). When using the all-eruption average conversion,
258   the total time-integrated forcing is only 75% of the IPCC AR5 total (-15233 MJ m^{-2}) (Figures
259   2b and c). Consequently, around 20-25% less energy has been lost from the climate system
260   due to volcanic radiative forcing between 500 BCE and 1900 CE than implied by the IPCC
261   AR5.

262   Figure 2d shows global annual-mean surface temperature anomalies calculated in a
263   simple climate model, FaIR (Finite Amplitude Impulse-Response simple climate-carbon-
264   cycle model) v1.4 (Millar et al., 2017; Smith et al., 2018a), forced with the three volcanic
265   forcing timeseries from Figure 2b. No other forcing agents are used such that the temperature
266   response is that from volcanic forcing only. To ensure that the climate is in balance long-term
267   and to avoid a long-term cooling trend, the volcanic forcing input to FaIR in Figure 2b is
268   adjusted such that the mean forcing over the timeseries is zero (resulting in small positive
269   ERF in volcanically-quiescent years). The simulated peak global mean surface cooling differs
270   by up to 0.4-0.5°C for the largest eruptions depending on the conversion used, demonstrating
271   that there are substantial uncertainties on the magnitude of past volcanic climate impacts. For
272   example, using the IPCC AR5 scaling, simulated peak global mean cooling following the

273   1257 Samalas eruption is 1.5°C (occurring in 1259) and for 1815 Mt. Tambora is -1.1°C
274   (occurring in 1816). Using the average conversion, the peak cooling is -1.0°C following
275   Samalas and -0.8°C following Tambora. For the ESP-dependent conversions, the peak
276   cooling is -1.1°C for Samalas and -0.9°C for Tambora. These predicted surface temperature
277   changes fall within the range of estimated cooling from proxy reconstructions; tree-ring
278   reconstructions of NH extratropical summer land cooling following 1257 Samalas and 1815
279   Mt. Tambora eruptions are −0.8°C to −1.3°C (Stoffel et al., 2015). A comparison of the
280   average global-mean cooling resulting from applying the different conversions across the
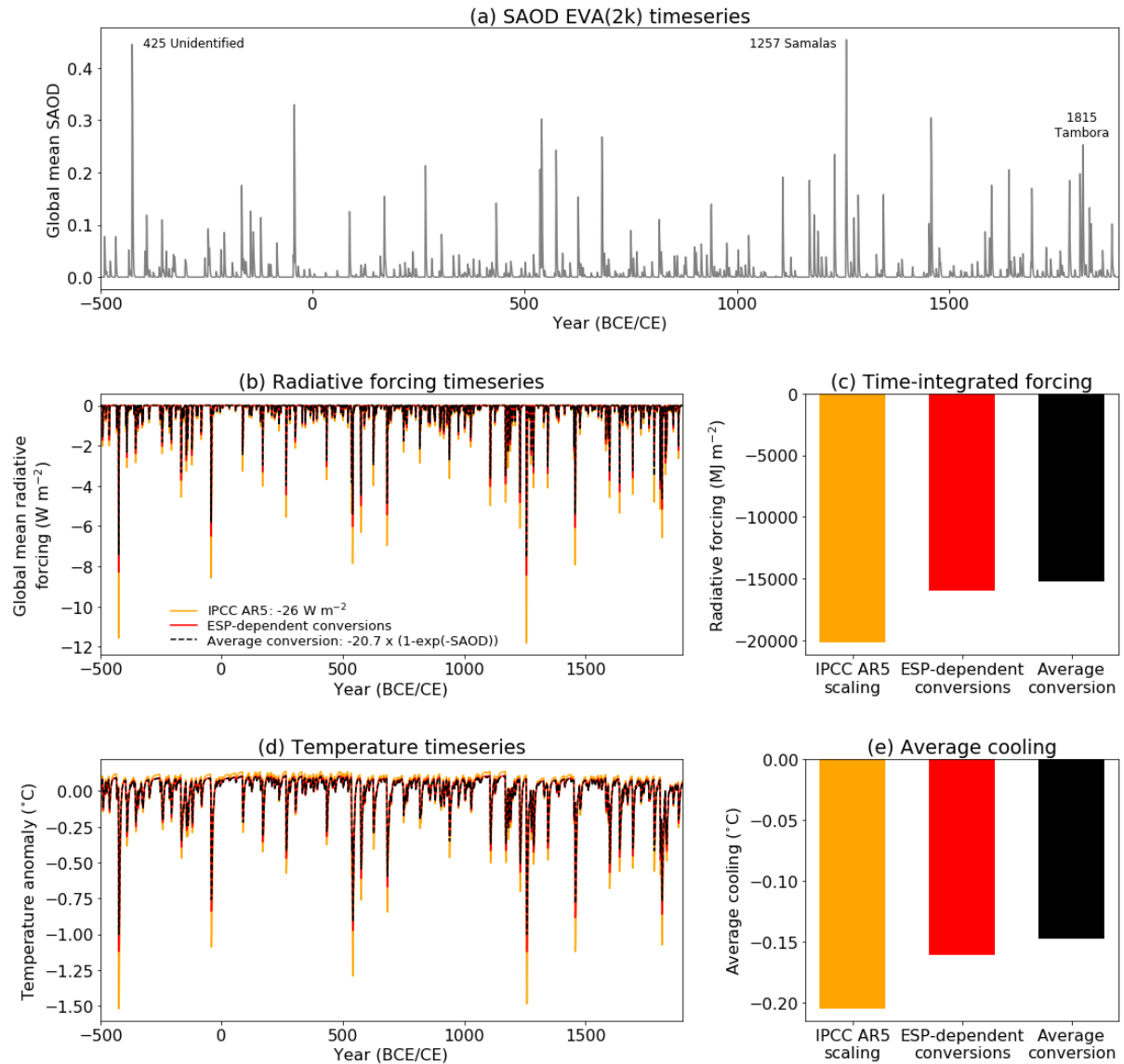281   whole timeseries is shown in Figure 2e.

282

283

284   **Figure 2. (a)** Global annual-mean volcanic SAOD timeseries from the EVA(2k)
285   reconstruction (calendar years), which does not include background sulfur emissions so that
286   SAOD represents the change due to volcanic eruptions only (b) Volcanic forcing calculated
287   from the SAOD using the IPCC AR5 scaling factor (orange), eruption source parameter
288   (ESP) dependent conversions (Table S1) (red) and the all-eruption average conversion
289   (black). (c) Time-integrated forcing from 500 BCE to 1900 CE for the three conversion
290   methods. (d) Global annual-mean surface temperature anomalies (relative to the 2400-year

291   average from each timeseries) calculated in a simple climate model (FaIR) for each volcanic
292   forcing timeseries. (e) The average cooling for temperature anomalies less than 0 for the three
293   conversion methods.

294

295   **3.2 The role of rapid adjustments**

296   In all simulations, the total global-mean rapid adjustments integrated over the duration
297   of the simulations are positive and therefore the ERF is less than the IRF. Figure 3 shows the
298   normalized time-integrated rapid adjustments (divided by the magnitude of the time-
299   integrated IRF so the sign is preserved) averaged over the different subsets of eruptions. On
300   average, the positive rapid adjustments reduce the volcanic forcing by 20% and are
301   dominated by a positive SW cloud adjustment (Figure 3g) driven by cloud changes that
302   reduce reflected SW radiation. It is not possible with our model diagnostics to attribute this
303   adjustment to specific cloud changes, but we do simulate a large reduction in high-level
304   clouds consistent with studies that investigated cloud changes due to sulfate geoengineering
305   (e.g., Krishnamohan et al., 2019; Kuebbeler et al., 2012; Visioni et al., 2018) and some
306   smaller changes to low-level clouds (Figure S5). Our result agrees with that of Gregory et al.
307   (2016) for SW cloud adjustments, who also investigated the radiative forcing from volcanic
308   eruptions. Their study did not diagnose the LW cloud adjustment. We find a small negative
309   LW adjustment from a reduction in cloud fraction (Figure 3h). In contrast, Schmidt et al.
310   (2018) found a positive net aerosol-cloud adjustment following eruptions in CESM1-
311   WACCM due to a positive LW aerosol-cloud interaction. This is further evidence that the
312   sign and magnitude of aerosol-cloud interactions following volcanic eruptions remain highly
313   uncertain and model dependent.

314   The remainder of the rapid adjustments are much smaller, although most are still
315   statistically significant (Student's t-test; stars in Figure 3). The spatial signatures of the rapid
316   adjustments are shown in Figures S6-S11. In general, the surface and tropospheric
317   temperature adjustments are positive (i.e., surface and tropospheric cooling leads to a
318   reduction in outgoing longwave radiation) and the stratospheric temperature adjustment is
319   negative (i.e., stratospheric warming following longwave absorption by the sulfate aerosols
320   leads to an increase in emissivity). The tropospheric temperature adjustment is strongest for
321   the NH eruptions and weakest for the SH eruptions likely because of the greater proportion of
322   land that can cool in the NH where the forcing occurs. The water vapor adjustment is both
323   positive and negative but is generally not statistically significant except for summer
324   eruptions. The water vapor adjustment reflects a balance between a decrease in tropospheric
325   water vapor due to cooling and an increase in stratospheric water vapor due to aerosol heating
326   (Dessler et al., 2013; Krishnamohan et al., 2019). The surface albedo adjustment is also
327   positive, reflecting changes in aerosol optical depth, snow cover and clouds.

328   The differences in the relationship between SAOD and ERF are predominantly due to
329   the differences in the magnitude of IRF outlined in section 3.1. However, we also find some
330   differences in the normalized total rapid adjustments and hence the ERF to IRF ratio,
331   depending on the ESPs, and the time since an eruption. For example, the proportion of the
332   IRF that is offset by the positive rapid adjustments is consistently larger for eruptions
333   occurring in January, regardless of the latitude (Figure 3a). For the January eruptions, the
334   rapid adjustments are ~23% of the IRF and ~17% of the IRF for the July eruptions. This is
335   mainly driven by the surface and tropospheric temperature adjustments, which are stronger
336   for the January eruptions (Figures 3b-c). Spatial plots of the tropospheric temperature
337   adjustment for January eruptions (Figures S6, S8, S10) show a large positive adjustment near

338   Greenland, suggesting that changes in circulation are driving this adjustment for eruptions in
339   both hemispheres.

340

341   The relative role of the total rapid adjustments (RA) also increases over time (see
342   Figure S12). For January eruptions RA/IRF is 19% in year 1, 24% in year 2 and 48% in year
343   3, although the forcing and rapid adjustments are extremely small and noisy in year 3 and are
344   therefore less important. The corresponding percentages for July eruptions are 16% (year 1)
345   18% (year 2) and 25% (year 3). The relative importance of all RA changes in each year and
346   in opposing directions and depends on the eruption month. The changing RA/IRF ratio is
347   therefore not attributable to a single adjustment and likely changes over time because of
348   different timescales and spatial patterns of the rapid adjustments that depend on the spatial
349   and microphysical evolution of the aerosol.
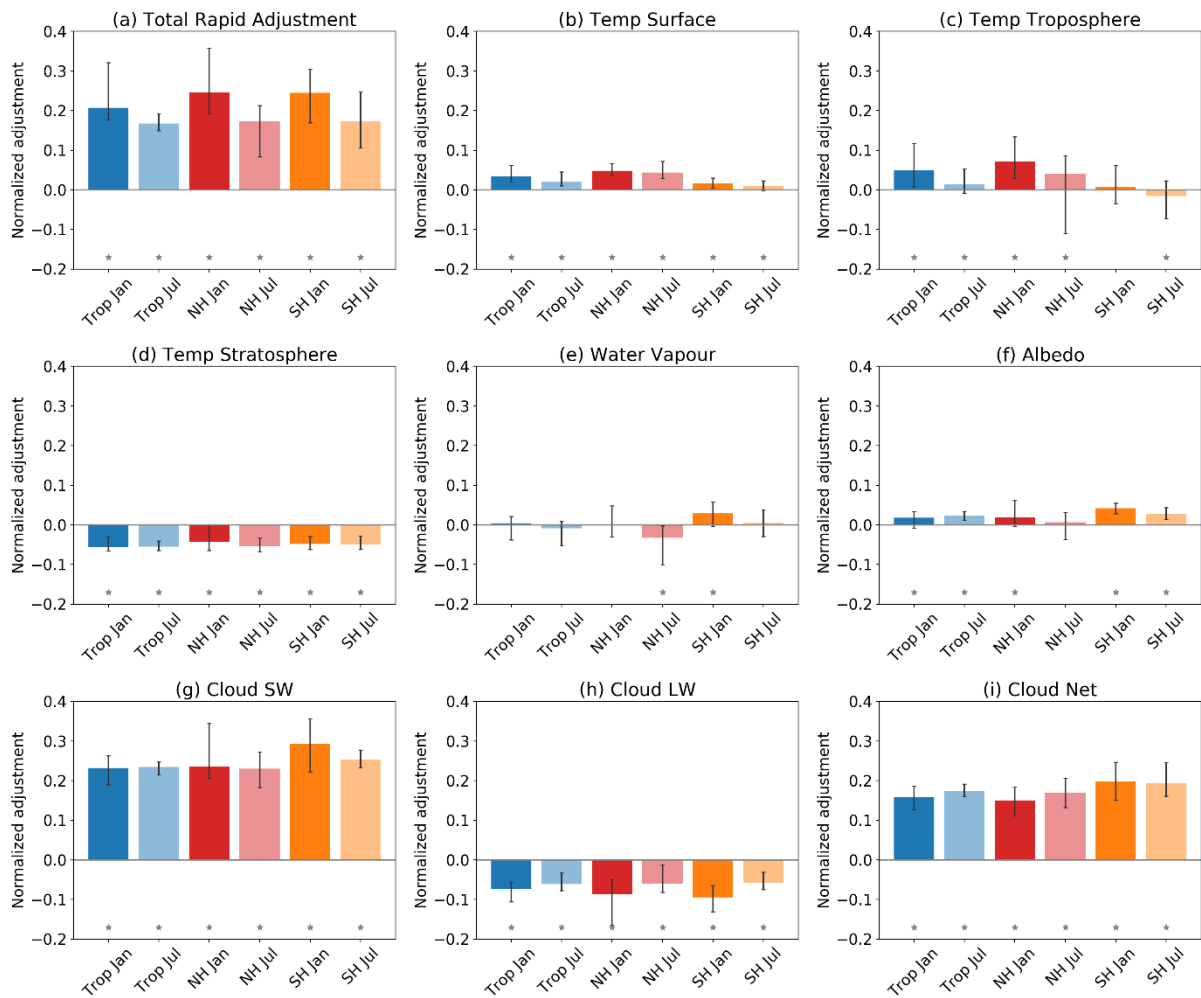
350

351

352 **Figure 3.** Time-integrated global-mean rapid adjustments (a-i) averaged across the different
353 eruption subsets. Rapid adjustments in each simulation were divided by the magnitude of the
354 time-integrated global-mean IRF (keeping positive rapid adjustments positive). The total
355 rapid adjustment is shown in Figure 3a and the remaining subplots show the breakdown of
356 the total rapid adjustment into the contributing components. Error bars show the range in the
357 rapid adjustments amongst the eruptions in each subset. Stars indicate where the adjustment
358 is significant at the 95% confidence level according to a two-sided Student's t-test.

Conclusions

360   The conversion between global-mean volcanic SAOD and global-mean ERF is an
361 important relationship to understand volcanic climate forcing efficiency, and required by
362 simple climate models that continue to underpin IPCC assessments.

363   Previous studies have focused on a limited number of eruptions to determine the
364 relationship between SAOD and volcanic radiative forcing. We have investigated this
365 relationship across aerosol-climate model simulations of a very wide range of eruptions with
366 different SO_2 emission magnitudes (10-100 Tg SO_2), latitudes (80°S-80°N), and for eruptions
367 in January and July. We have shown that the SAOD to ERF relationship is non-unique and
368 varies widely depending on the aerosol distribution and incoming solar radiation and
369 consequently the time after an eruption, eruption season and eruption latitude. For eruption
370 categories investigated here, forcing per unit of SAOD is weaker in the first year following an
371 eruption than in years 2 and 3, is stronger for tropical eruptions than extratropical eruptions
372 and stronger for winter eruptions than summer eruptions.

373   We find that the average scaling factor (across all eruption categories) between SAOD
374 and ERF is -17.0 ± 0.2 W m^{-2}, which is considerably lower than the factor of -26 W m^{-2} per
375 unit SAOD used by IPCC AR5. In our study this is because positive rapid adjustments
376 dominated by a positive shortwave cloud adjustment act to reduce the volcanic forcing; the
377 ERF is on average 20% less than the instantaneous radiative forcing (IRF). Total rapid
378 adjustments are on average stronger for January eruptions regardless of eruption latitude,
379 offsetting ~23% of the IRF compared to ~17% for the July eruptions due to a larger surface
380 and tropospheric temperature adjustment that occurs for January eruptions. Our results
381 provide evidence that uncertainty in volcanic forcing estimates based on volcanic SAOD and
382 therefore volcanic climatic impacts is large. Our results also suggest that volcanic forcing has
383 been previously overestimated, which has implications for transient energy balance
384 calculations used to constrain the transient climate response and equilibrium climate
385 sensitivity. For example, we find that the time-integrated volcanic ERF for eruptions between
386 500 BCE and 1900 CE is around 20% less than that based on the IPCC AR5 scaling factor
387 with resulting differences in peak global-mean surface cooling following the largest eruptions
388 of up to 0.4°C.

389   We provide several conversions between global annual-mean volcanic SAOD (in the
390 form of 1-e^{-SAOD}) and ERF (Figure 1, Table S1). These conversions do not account for all
391 variability we find in the relationship between SAOD and ERF, and which may also vary
392 depending on the model used and atmospheric background state, but provide a considerable
393 improvement on the single scaling factor as used by IPCC AR5.

394
395

Acknowledgments

Summary model data are currently being uploaded to the CEDA archive and are in the supporting information (Tables S2-S15).

References

Andersson, S. M., Martinsson, B. G., Vernier, J. P., Friberg, J., Brenninkmeijer, C. A. M., Hermann, M., et al. (2015). Significant radiative impact of volcanic aerosol in the lowermost stratosphere. *Nature Communications, 6*. 10.1038/ncomms8692

Aubry, T. J., Toohey, M., Marshall, L., Schmidt, A., & Jellinek, A. M. (2020). A new volcanic stratospheric sulfate aerosol forcing emulator (EVA_H): Comparison with interactive stratospheric aerosol models. *Journal of Geophysical Research: Atmospheres*, 125, e2019JD031303. 10.1029/2019JD031303

Crowley, T., & Unterman, M. B. (2013). Technical details concerning development of a 1200 yr proxy index for global volcanism. *Earth System Science Data, 5*(1), 187-197. 10.5194/essd-5-187-2013

Dessler, A. E., Schoeberl, M. R., Wang, T., Davis, S. M., & Rosenlof, K. H. (2013). Stratospheric water vapor feedback. *Proceedings of the National Academy of Sciences, 110*(45), 18087. 10.1073/pnas.1310344110

Edwards, J. M., & Slingo, A. (1996). Studies with a flexible new radiation code .1. Choosing a configuration for a large-scale model. *Quarterly Journal of the Royal Meteorological Society, 122*(531), 689-719. 10.1002/qj.49712253107

Forster, P. M., Andrews, T., Good, P., Gregory, J. M., Jackson, L. S., & Zelinka, M. (2013). Evaluating adjusted forcing and model spread for historical and future scenarios in the CMIP5 generation of climate models. *Journal of Geophysical Research: Atmospheres, 118*(3), 1139-1150. 10.1002/jgrd.50174

Forster, P. M., Richardson, T., Maycock, A. C., Smith, C. J., Samset, B. H., Myhre, G., et al. (2016). Recommendations for diagnosing effective radiative forcing from climate models for CMIP6. *Journal of Geophysical Research: Atmospheres, 121*(20), 12,460-412,475. 10.1002/2016JD025320

Gao, C., Robock, A., & Ammann, C. (2008). Volcanic forcing of climate over the past 1500 years: An improved ice core-based index for climate models. *Journal of Geophysical Research-Atmospheres, 113*(D23). Article. 10.1029/2008jd010239

Gregory, J. M., Andrews, T., Ceppi, P., Mauritsen, T., & Webb, M. J. (2019). How accurately can the climate sensitivity to CO2 be estimated from historical climate change? *Climate Dynamics*. 10.1007/s00382-019-04991-y

Gregory, J. M., Andrews, T., Good, P., Mauritsen, T., & Forster, P. M. (2016). Small global-mean cooling due to volcanic radiative forcing. *Climate Dynamics, 47*(12), 3979-3991. 10.1007/s00382-016-3055-1

Guo, S., Rose, W. I., Bluth, G. J. S., & Watson, I. M. (2004). Particles in the great Pinatubo volcanic cloud of June 1991: The role of ice. *Geochemistry Geophysics Geosystems, 5*. 10.1029/2003gc000655

449 Hansen, J., Sato, M., Ruedy, R., Nazarenko, L., Lacis, A., Schmidt, G. A., et al. (2005). Efficacy of climate
450   forcings. *Journal of Geophysical Research-Atmospheres, 110*(D18). Review. 10.1029/2005jd005776
451 Haustein, K., Otto, F. E. L., Venema, V., Jacobs, P., Cowtan, K., Hausfather, Z., et al. (2019). A Limited Role
452   for Unforced Internal Variability in Twentieth-Century Warming. *Journal of Climate, 32*(16), 4893-
453   4917. 10.1175/jcli-d-18-0555.1
454 Krishnamohan, K. P. S. P., Bala, G., Cao, L., Duan, L., & Caldeira, K. (2019). Climate system response to
455   stratospheric sulfate aerosols: sensitivity to altitude of aerosol layer. *Earth Syst. Dynam., 10*(4), 885-
456   900. 10.5194/esd-10-885-2019
457 Kuebbeler, M., Lohmann, U., & Feichter, J. (2012). Effects of stratospheric sulfate aerosol geo-engineering on
458   cirrus clouds. *Geophysical Research Letters, 39*(23). 10.1029/2012gl053797
459 Landwehrs, J. P., Feulner, G., Hofmann, M., & Petri, S. (2020). Climatic fluctuations modeled for carbon and
460   sulfur emissions from end-Triassic volcanism. *Earth and Planetary Science Letters, 537*, 116174.
461   doi.org/10.1016/j.epsl.2020.116174
462 Larson, E. J. L., & Portmann, R. W. (2016). A Temporal Kernel Method to Compute Effective Radiative
463   Forcing in CMIP5 Transient Simulations. *Journal of Climate, 29*(4), 1497-1509. 10.1175/JCLI-D-15-
464   0577.1
465 Mann, G. W., Carslaw, K. S., Spracklen, D. V., Ridley, D. A., Manktelow, P. T., Chipperfield, M. P., et al.
466   (2010). Description and evaluation of GLOMAP-mode: a modal global aerosol microphysics model for
467   the UKCA composition-climate model. *Geoscientific Model Development, 3*(2), 519-551.
468   10.5194/gmd-3-519-2010
469 Manners, J., Edwards, J. M., Hill, P., & Thelen, J. C. (2015). *SOCRATES (Suite Of Community RAdiative
470   Transfer codes based on Edwards and Slingo) technical guide*. Met Office, UK.
471 Marshall, L., Johnson, J. S., Mann, G. W., Lee, L., Dhomse, S. S., Regayre, L., et al. (2019). Exploring How
472   Eruption Source Parameters Affect Volcanic Radiative Forcing Using Statistical Emulation. *Journal of
473   Geophysical Research: Atmospheres, 124*, 964– 985. 10.1029/2018JD028675
474 Marshall, L., Schmidt, A., Toohey, M., Carslaw, K. S., Mann, G. W., Sigl, M., et al. (2018). Multi-model
475   comparison of the volcanic sulfate deposition from the 1815 eruption of Mt. Tambora. *Atmospheric
476   Chemistry and Physics, 18*(3), 2307-2328. 10.5194/acp-18-2307-2018
477 Millar, R. J., Nicholls, Z. R., Friedlingstein, P., & Allen, M. R. (2017). A modified impulse-response
478   representation of the global near-surface air temperature and atmospheric concentration response to
479   carbon dioxide emissions. *Atmos. Chem. Phys., 17*(11), 7213-7228. 10.5194/acp-17-7213-2017
480 Myhre, G., Shindell, D., Bréon, F.-M., Collins, W., Fuglestvedt, J., Huang, J., et al. (2013). Anthropogenic and
481   Natural Radiative Forcing. In T. F. Stocker, D. Qin, G. K. Plattner, M. Tignor, S. K. Allen, J.
482   Boschung, A. Nauels, Y. Xia, V. Bex, & P. M. Midgley (Eds.), *Climate Change 2013: The Physical
483   Science Basis. Contribution of Working Group I to the Fifth Assessment Report of the
484   Intergovernmental Panel on Climate Change*. Cambridge, United Kingdom and New York, NY, USA.:
485   Cambridge University Press.
486 Schmidt, A., Mills, M. J., Ghan, S., Gregory, J. M., Allan, R. P., Andrews, T., et al. (2018). Volcanic Radiative
487   Forcing From 1979 to 2015. *Journal of Geophysical Research: Atmospheres, 123*(22), 12,491-412,508.
488   10.1029/2018jd028776
489 Schurer, A. P., Hegerl, G. C., Mann, M. E., Tett, S. F. B., & Phipps, S. J. (2013). Separating Forced from
490   Chaotic Climate Variability over the Past Millennium. *Journal of Climate, 26*(18), 6954-6973.
491   10.1175/jcli-d-12-00826.1
492 Shell, K. M., Kiehl, J. T., & Shields, C. A. (2008). Using the Radiative Kernel Technique to Calculate Climate
493   Feedbacks in NCAR's Community Atmospheric Model. *Journal of Climate, 21*(10), 2269-2282.
494   10.1175/2007JCLI2044.1
495 Sherwood, S. C., Bony, S., Boucher, O., Bretherton, C., Forster, P. M., Gregory, J. M., & Stevens, B. (2015).
496   Adjustments in the Forcing-Feedback Framework for Understanding Climate Change. *Bulletin of the
497   American Meteorological Society, 96*(2), 217-228. 10.1175/BAMS-D-13-00167.1
498 Sigl, M., Winstrup, M., McConnell, J. R., Welten, K. C., Plunkett, G., Ludlow, F., et al. (2015). Timing and
499   climate forcing of volcanic eruptions for the past 2,500 years. *Nature, 523*(7562), 543–549.
500   10.1038/nature14565
501 Smith, C. J., Forster, P. M., Allen, M., Fuglestvedt, J., Millar, R. J., Rogelj, J., & Zickfeld, K. (2019).
502   Current fossil fuel infrastructure does not yet commit us to 1.5 °C warming. *Nature Communications,
503   10*(1), 101. 10.1038/s41467-018-07999-w
504 Smith, C. J., Forster, P. M., Allen, M., Leach, N., Millar, R. J., Passerello, G. A., & Regayre, L. A. (2018a).
505   FAIR v1.3: a simple emissions-based impulse response and carbon cycle model. *Geosci. Model Dev.,
506   11*(6), 2273-2297. 10.5194/gmd-11-2273-2018

507   Smith, C. J., Kramer, R. J., Myhre, G., Forster, P. M., Soden, B. J., Andrews, T., et al. (2018b). Understanding
508   Rapid Adjustments to Diverse Forcing Agents. *Geophysical Research Letters, 45*(21), 12,023-012,031.
509   10.1029/2018GL079826
510   Smith, C. J., Kramer, R. J., & Sima, A. (2020). The HadGEM3-GA7.1 radiative kernel: the importance of a
511   well-resolved stratosphere. *Earth Syst. Sci. Data Discuss., 2020*, 1-16. 10.5194/essd-2019-254
512   Soden, B. J., Held, I. M., Colman, R., Shell, K. M., Kiehl, J. T., & Shields, C. A. (2008). Quantifying Climate
513   Feedbacks Using Radiative Kernels. *Journal of Climate, 21*(14), 3504-3520. 10.1175/2007JCLI2110.1
514   Stoffel, M., Khodri, M., Corona, C., Guillet, S., Poulain, V., Bekki, S., et al. (2015). Estimates of volcanic-
515   induced cooling in the Northern Hemisphere over the past 1,500 years. *Nature Geoscience, 8*(10), 784-
516   788. 10.1038/ngeo2526
517   Taylor, K. E., Crucifix, M., Braconnot, P., Hewitt, C. D., Doutriaux, C., Broccoli, A. J., et al. (2007). Estimating
518   Shortwave Radiative Forcing and Response in Climate Models. *Journal of Climate, 20*(11), 2530-2543.
519   10.1175/JCLI4143.1
520   Timmreck, C., Mann, G. W., Aquila, V., Hommel, R., Lee, L. A., Schmidt, A., et al. (2018). The Interactive
521   Stratospheric Aerosol Model Intercomparison Project (ISA-MIP): motivation and experimental design.
522   *Geoscientific Model Development, 11*(7), 2581-2608. 10.5194/gmd-11-2581-2018
523   Toohey, M., Kruger, K., Niemeier, U., & Timmreck, C. (2011). The influence of eruption season on the global
524   aerosol evolution and radiative impact of tropical volcanic eruptions. *Atmospheric Chemistry and
525   Physics, 11*(23), 12351-12367. 10.5194/acp-11-12351-2011
526   Toohey, M., Kruger, K., & Timmreck, C. (2013). Volcanic sulfate deposition to Greenland and Antarctica: A
527   modeling sensitivity study. *Journal of Geophysical Research-Atmospheres, 118*(10), 4788-4800.
528   10.1002/jgrd.50428
529   Toohey, M., & Sigl, M. (2017). Volcanic stratospheric sulfur injections and aerosol optical depth from 500 BCE
530   to 1900 CE. *Earth System Science Data, 9*(2), 809-831. 10.5194/essd-9-809-2017
531   Toohey, M., Stevens, B., Schmidt, H., & Timmreck, C. (2016). Easy Volcanic Aerosol (EVA v1.0): an idealized
532   forcing generator for climate simulations. *Geoscientific Model Development, 9*(11), 4049-4070.
533   10.5194/gmd-9-4049-2016
534   Visioni, D., Pitari, G., di Genova, G., Tilmes, S., & Cionni, I. (2018). Upper tropospheric ice sensitivity to
535   sulfate geoengineering. *Atmos. Chem. Phys., 18*(20), 14867-14887. 10.5194/acp-18-14867-2018
536   Walters, D. N., Williams, K. D., Boutle, I. A., Bushell, A. C., Edwards, J. M., Field, P. R., et al. (2014). The
537   Met Office Unified Model Global Atmosphere 4.0 and JULES Global Land 4.0 configurations.
538   *Geoscientific Model Development, 7*(1), 361-386. 10.5194/gmd-7-361-2014
539   Wetherald, R. T., & Manabe, S. (1988). Cloud Feedback Processes in a General Circulation Model. *Journal of
540   the Atmospheric Sciences, 45*(8), 1397-1416. 10.1175/1520-0469(1988)045<1397:CFPIAG>2.0.CO;2
541   Zanchettin, D., Khodri, M., Timmreck, C., Toohey, M., Schmidt, A., Gerber, E. P., et al. (2016). The Model
542   Intercomparison Project on the climatic response to Volcanic forcing (VolMIP): experimental design
543   and forcing input data for CMIP6. *Geoscientific Model Development, 9*(8), 2701-2719. 10.5194/gmd-9-
544   2701-2016
545
546